Journal of Energy Storage 154 (2026) 121329

Contents lists available at ScienceDirect

Journal of Energy Storage

journal homepage: www.elsevier.com/locate/est

Research papers

Conjugated microporous polymers incorporated redox-active hexaazatrinaphtylene and triphenyltrazine moieties for efficient faradaic supercapacitor energy storage

Mohamed Gamal Mohamed [a,b,*,1], Mohsin Ejaz [a,1], Abdul Basit [a], Yang-Chin Kao [a], Ahmed A.K. Mohammed [b], Shiao-Wei Kuo [a,c,*]

[a] Department of Materials and Optoelectronic Science, Center for Functional Polymers and Supramolecular Materials, National Sun Yat-Sen University, Kaohsiung, 804, Taiwan
[b] Chemistry Department, Faculty of Science, Assiut University, Assiut, 71515, Egypt
[c] Department of Medicinal and Applied Chemistry, Kaohsiung Medical University, Kaohsiung, 807, Taiwan

ARTICLE INFO

Keywords:
Conjugated microporous polymer
Triazine
Hexaazatrinaphtylene
Redox-active
Symmetric device
Faradaic supercapacitor

ABSTRACT

Conjugated microporous polymers (CMPs) have attracted considerable attention owing to their microporous structures and versatile physicochemical behavior, combined with π-conjugated frameworks. However, their practical application in electric storage devices, such as supercapacitors, is hindered by their inherently low electronic conductivity and limited redox-active functionality, which limit specific capacitance and charge–discharge stability. Addressing these challenges, this study introduces two novel redox-active conjugated CMPs based on hexaazatrinaphtylene (HATN), namely TPA-HATN-CMP and TPT-HATN-CMP. These materials were synthesized Suzuki coupling polymerization of 2,8,14-tribromodiquinoxalino[2,3-a:2′,3′-c]phenazine (HATN-Br_3), tris(4-bromophenyl)amine (TPA-Br_3), tris(4-bromophenyl)-1,3,5-triazine (TPT-Br_3), and 1,4-phenylenediboronic acid (pH-2BO). The resulting TPA-HATN-CMP and TPT-HATN-CMP demonstrated remarkable thermal stability, with T_{d10} values of 633 and 679 °C, and high surface areas of 459 and 428 $m^2\ g^{-1}$, respectively. The incorporation of redox-active HATN units into the CMP backbone significantly enhanced their charge mobility, faradaic charge capabilities, and electron transfer efficiency. In a three-electrode configuration, the TPT-HATN-CMP achieved an impressive specific capacitance of 505 F g^{-1} along with exceptional capacitance stability of 96.8% after 5000 cycles. The symmetric two-electrode supercapacitor assembled with TPT-HATN-CMP delivers a specific capacitance of 219.4 F g^{-1} and an energy density of 22.01 Wh kg^{-1} at 0.85 V. Moreover, the device exhibited excellent cycling stability, maintaining 80% of its initial capacitance after 5000 successive cycles. The results obtained underscore the suitability of HATN-CMPs as effective electrodes for superior energy storage performance.

1. Introduction

With increasing concerns about the long-term environmental impacts of fossil fuel consumption, there is a growing emphasis on advancing research and development in alternative energy solutions [1,2]. Electrochemical energy storage systems have emerged as vital tools in addressing global energy deficits [3]. Among these, supercapacitors (SCs) have gained attention as efficient electrical energy storage devices owing to their efficient charge–discharge characteristics, superior power density, and an enhanced operational lifetime relative to conventional energy storage capacitors [4–8]. Typically, supercapacitors (SCs) are grouped into two types—pseudocapacitors and electric double-layer capacitors—according to their respective charge storage behaviors [4–8]. In EDLCs, energy storage depends on the reversible interaction of ions with the electrode surface. By contrast, pseudocapacitors rely on fast, reversible Faradaic redox reactions occurring between electrolyte and electrodes [4–8]. Carbon-based materials are widely used in SCs and store charge through EDLC. However,

* Corresponding authors at: Department of Materials and Optoelectronic Science, Center for Functional Polymers and Supramolecular Materials, National Sun Yat-Sen University, Kaohsiung, 804, Taiwan.
E-mail addresses: mgamal.eldin12@yahoo.com, mgamal.eldin12@mail.nsysu.edu.tw (M.G. Mohamed), kuosw@faculty.nsysu.edu.tw (S.-W. Kuo).
[1] These authors contributed equally to this work.

https://doi.org/10.1016/j.est.2026.121329
Received 11 November 2025; Received in revised form 2 February 2026; Accepted 24 February 2026
Available online 3 March 2026

they are limited by low energy density and specific capacitance [9,10]. Redox-active materials can store charge through reversible faradaic reactions [11–14]. Despite this advantage, the rapid redox processes often lead to electrode expansion and contraction, which compromises mechanical stability and restricts access to active regions [15]. Additionally, their relatively poor rate capability, low electrical conductivity, and limited cycling durability pose challenges for practical applications [16]. Conductive polymers integrating carbon-based materials with pseudocapacitive components have shown promise as electrode materials for SCs [17,18]. However, these approaches often result in only marginal improvements in performance [19]. To address these challenges and enhance SCs' performance, it is crucial to develop innovative materials for electrodes that possess excellent conductivity, adjustable porous structures, long-term stability, and inherent redox-active properties. Porous materials are typically preferred over nonporous ones due to their increased surface area and porosity, which enable access to active sites. [20–24]. Among these materials, CMPs obtained significant attention attributed to their versatile applications in energy technology and environmental protection fields [25–27]. CMPs are composed of interconnected 3D porous networks characterized by pores typically smaller than 2 nm. CMPs have attractive characteristics like π-conjugation, high surface area, robust stability, ordered micropores, tunable properties, and versatile functionalization [28–30]. These advantages highlight the potential of CMPs across different applications, such as catalysis, luminescence, environmental remediation, energy storage, and optical uses [31–34]. In the realm of electrochemistry, CMPs exhibit distinctive properties compared to traditional polymers. Their ability to incorporate redox-active units allows for tailored electrochemical behavior [35]. Furthermore, their porous nature ensures maximum exposure of heteroatomic active sites, facilitating rapid ion diffusion and mitigating issues related to random folding [36–38]. As a result, CMPs are considered promising candidates for high-capacity electrochemical energy storage. However, CMPs face challenges such as limited cycling stability and low electronic conductivity, which hinder their practical performance [39,40]. To address these limitations, researchers have explored strategies such as integrating redox-active units, such as anthraquinone, pyridine, triphenyltriazine (TPT), and triphenylamine (TPA) into CMP frameworks, leading to notable improvements in supercapacitor performance [41–49]. Additionally, the porous structure of CMPs facilitates efficient electrolyte ion transport, enhancing interactions between active sites and electrolytes. Despite the progress in developing pseudocapacitive CMPs, their performance in supercapacitor applications remains suboptimal. To advance this field, there is a pressing need for pseudocapacitive CMPs with improved activity and physicochemical stability, which could drive further innovation and development in energy storage technologies.

Phenazine-based redox materials have received considerable interest for energy-storage applications because they undergo reversible faradaic reactions that contribute to high capacity and stability [50–52]. The hexaazatrinaphthylene (HATN), a phenazine-derived redox-active compound with a highly conjugated π-system and multiple nitrogen sites, has been widely investigated for various energy storage applications. Its unique molecular structure enables efficient electron transfer, multiple redox states, and excellent electrochemical reversibility [53,54]. For example, Guan et al. synthesized a new azo-based HATN porous material as a stable cathode for lithium-ion batteries, delivering high capacity, fast ion transport, and superior cycling stability [55]. A cobalt-based coordination polymer, Co(HAT-CN), was synthesized and combined with graphene oxide to improve conductivity and cycling stability for batteries having high capacity and excellent structural stability [56]. Our group prepared HATN-based CMP, delivering a capacitance of 1790 F g^{-1} as a supercapacitor electrode [57]. Zhu et al. used HATN to synthesize HPOP-1 for SCs, delivering a capacitance of 667 F g^{-1}, having high pseudocapacitance [58]. Similarly, triphenylamine (TPA) and triphenyltriazine (TPT) are also redox-active monomers that are essential for designing π-conjugated frameworks for energy storage [59,60]. Our group reported a TPA-linked CMP (TPA-TAB) with a high surface area, and at 0.5 A g^{-1}, this material, which has a specific capacitance of 684 F g^{-1}, demonstrates remarkable performance for SCs [61]. Lee et al. synthesized triazine-linked COFs (TPDA-COF) and combined them with carbon nanotubes, producing materials endowed with redox activity, high surface area, and enhanced charge transfer capability for supercapacitors [62]. Qiu et al. fabricated grid-like triazine-based porous materials (TCOPs) with tunable cavities, with ultrahigh capacitance of 8412 F g^{-1}, outperforming previously reported aqueous SCs. Their outstanding performance is attributed to abundant accessible redox-active sites and strong interactions with the electrolyte [63]. Although CMPs incorporating these redox-active units individually have demonstrated promising capacitance, systematic investigations that isolate the intrinsic role of nitrogen enrichment within structurally comparable CMP frameworks are still lacking.

In this work, the main research idea of this work is to establish a controlled conjugated porous framework to elucidate the influence of overall nitrogen content on pseudocapacitive behavior while minimizing structural interference. To achieve this, two pseudocapacitive CMPs, namely TPA-HATN-CMP and TPT-HATN-CMP, were prepared via a Suzuki coupling reaction. The reaction utilized HATN-Br_3, TPA-Br_3, TPT-Br_3, and 1,4-phenylenediboronic acid (pH-2BO) as key building blocks. The combination of redox-active HATN-Br_3, TPA-Br_3, and TPT-Br_3 moieties to prepare CMPs has not been previously explored or reported for supercapacitor applications. This strategy enables the development of CMPs with highly comparable conjugated backbones, pore architecture, and surface areas, while systematically modulating nitrogen density within the framework. The two CMPs were purposefully constructed with nearly identical conjugated and porous frameworks to develop structural effects and thereby elucidate the role of nitrogen content in supercapacitive charge storage. Incorporation of HATN with either TPA or TPT maintains a comparable network topology while enabling precise modulation of nitrogen density and electronic structure. Both materials exhibit pseudocapacitive characteristics derived from redox-active nitrogen sites embedded within π-conjugated backbones, allowing faradaic and electric double-layer charge storage. Despite these structural similarities, distinct electrochemical behaviors are observed. The nitrogen–enriched TPT-HATN-CMP demonstrates intensified redox activity and a higher pseudocapacitive contribution, whereas the TPA-HATN-CMP benefits from enhanced electronic donation and accelerated charge-transfer kinetics, leading to superior rate performance and long-term cycling stability. The redox-active components within these HATN-CMPs facilitate electron transfer reactions, which significantly enhance the material's pseudocapacitive performance. These findings highlight molecular-level nitrogen engineering within structurally analogous porous frameworks for supercapacitor performance and provide clear design principles for advanced redox-active CMPs.

2. Experimental section

2.1. Materials

4-Bromobenzene-1,2-diamine (4-Br$BzNH_2$), N-bromosuccinimide (NBS, 99%), triphenylamine (TPA), tetrakis(triphenylphosphine)palladium(0) [$Pd(PPh_3)_4$], trifluoromethanesulfonic acid, 4-bromobenzonitrile, acetic acid (AcOH), cyclohexanone octahydrate, 1,4-phenylenediboronic acid (pH-2BO), potassium carbonate (K_2CO_3), 1,4-dioxane (DO), and dimethylformamide (DMF) were procured from Sigma-Aldrich.

2.2. Synthesis of HATN-Br_3

A mixture containing 4-Br$BzNH_2$ (4 g, 21.38 mmol) was prepared in 140 mL of acetic acid. Cyclohexanone octahydrate (2.27 g, 7.13 mmol) was then added to the reaction system and refluxed at 120 °C for one day

in a nitrogen environment with consistent agitation. Upon completion, the material was collected by vacuum filtration and purified through successive rinsing steps involving deionized water, ethanol, and hot acetic acid. The green powder obtained was further treated oxidatively by mixing in 60 mL of 35 wt% nitric acid at 120 °C for 3 h. A yellow solid, referred to as HATN-Br_3, was ultimately acquired. FTIR (KBr, cm^{-1}): 3067.6, (C—H aromatic), 1613 (C=N), 1514 (C=C), and 1249 (C—N) [**Fig. S1**]. High-resolution FT-MS (*m/z*): calcd for ($C_{24}H_9Br_3N_6$), 621.09; found, 621.8403.

2.3. Synthesis of TPA-Br_3

The mixture of triphenylamine (5 g, 4.08 mmol) and DMF (100 mL) was placed in an ice bath and stirred magnetically overnight. Subsequently, the mixture of N-bromosuccinimide (NBS, 12 g, 12.32 mmol) in DMF (50 mL) was added dropwise under constant stirring [**Scheme S1**]. After completion of the reaction, the crude product was extracted with DCM to afford TPA-Br_3 as a white powder.

2.4. Synthesis of TPT-Br_3

In an ice bath maintained at 0 °C, 4-bromobenzonitrile (1.77 g, 9.72 mmol) was introduced into anhydrous $CHCl_3$ (55 mL). Trifluoromethanesulfonic acid (4.72 mL) was then introduced dropwise with continuous stirring for 40 min, then allowed to reach room temperature and stir for a day; the mixture was then added to ice water (60 mL) [**Scheme S2**]. The Na_2CO_3 was used as a neutralizing agent, and the solid product was collected by filtration and kept under vacuum for 7 h to remove residual solvent to afford TPT-Br_3 as a white solid.

2.5. Synthesis of TPA and TPT-based HATN-CMP

To synthesize TPA-HATN-CMP, a 30 mL Schlenk tube was charged with TPA-Br_3 (0.20 g, 0.414 mmol), HATN-Br_3 (0.15 g, 0.241 mmol), pH-2BO (0.32 g, 1.93 mmol), and $Pd(PPh_3)_4$ (0.05 g, 0.04 mmol) in 20 mL of DMF, along with 5 mL of a 2 M aqueous K_2CO_3 solution. The mixture was heated at 110 °C for 72 h. TPT-HATN-CMP was synthesized under identical conditions, using TPT-Br_3 (0.20 g, 0.36 mmol). HATN-Br_3 (0.132 g, 0.212 mmol), pH-2BO (0.29 g, 1.74 mmol), and $Pd(PPh_3)_4$ (0.05 g, 0.04 mmol). After cooling, the resulting solids were collected and sequentially washed three times with DMF, methanol, acetone, and THF, affording a brown solid product.

3. Results and discussion

3.1. Preparation and characterization of TPA and TPT-based HATN-CMP

The preparation of the essential monomers, namely TPA-Br_3, HATN-Br_3, and TPT-Br_3, was accomplished through a stepwise synthetic route [Fig. 1]. TPA-Br_3 was obtained in excellent yield by brominating TPA with NBS in DMF at 100 °C [Fig. 1(a)**, Scheme S1**]. TPA-Br_3 shows a doublet of doublet aromatic proton signals at 7.34–7.36 ppm and 6.91–6.93 ppm in **Fig. S2(a)**. In the ^{13}C NMR spectrum, TPA-Br_3 displays aromatic carbon signals in the range of 116–146 ppm in **Fig. S2(b)**. HATN-Br_3 was produced as a yellow solid with high purity and yield by condensing 4-$BrBzNH_2$ with cyclohexanone in acetic acid at 120 °C [Fig. 1(b)]. The FTIR spectrum of HATN-Br_3 shows peaks at 3067.6, 1613, 1514, and 1249 representing C—H aromatic, C=N, C=C, and C—N, respectively [**Fig. S1**]. For TPT-Br_3, the synthesis involved treating 4-bromobenzonitrile with TMSA at 0 °C for 24 h [Fig. 1(c)**, Scheme S2**]. TPT-Br_3 exhibits a doublet of doublet aromatic proton signals at 8.59–8.61 ppm and 7.70–7.72 ppm. This shift is attributed to the electron-withdrawing effect of the triazine unit, which deshields the aromatic protons, as shown in **Fig. S3(a)**. while TPT-Br_3 shows aromatic carbon signals between 127 and 134 ppm. Additionally, the carbon of the triazine unit in TPT-Br_3 appears at 171 ppm in **Fig. S3(b)**. Finally, TPA-HATN-CMP [Fig. 1(d)] and TPT-HATN-CMP [Fig. 1(e)], were assembled through Suzuki coupling of HATN-Br_3 and pH-2BO with TPA-Br_3 or TPT-Br_3, respectively, in DMF with 2 M K_2CO_3 as solvents. These

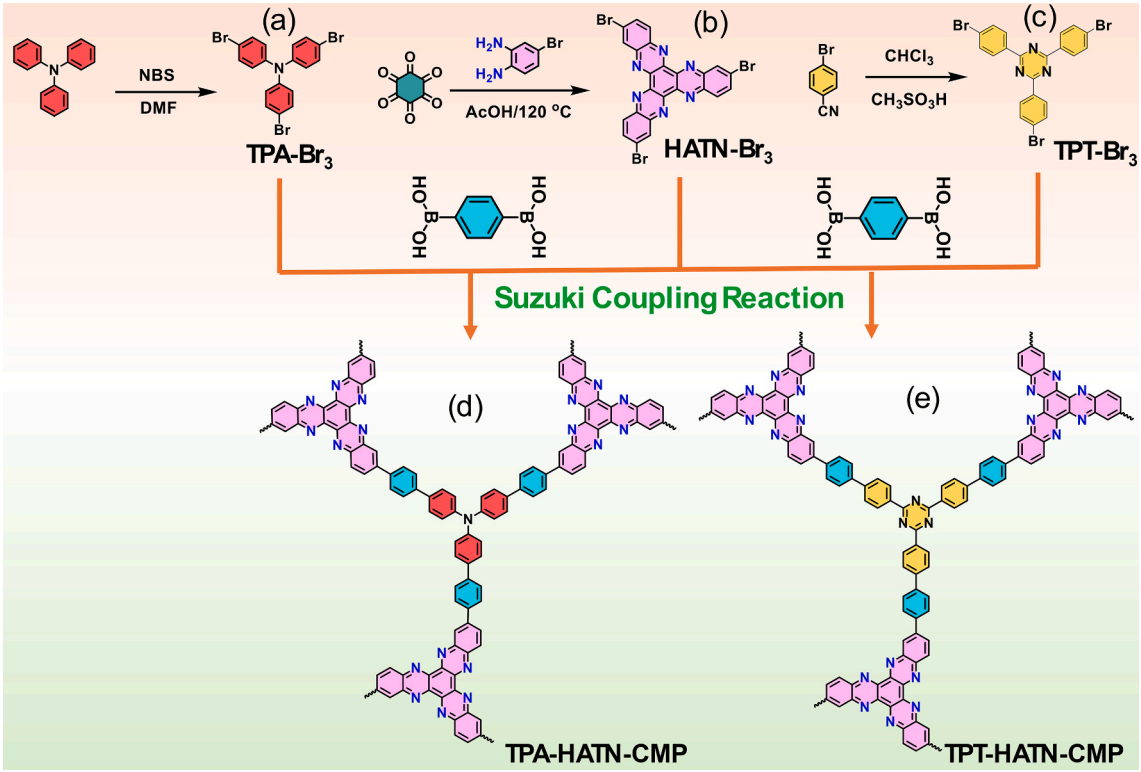

Fig. 1. Schematic representation of (a) TPA-Br_3, (b) HATN-Br_3, (c) TPT-Br_3, (d) TPA-HATN-CMP, and (e) TPT-HATN-CMP.

dark brown powders feature the electroactive HATN core, known for its abundance of redox-responsive functional groups, which contribute significantly to enhanced electrochemical behavior [57,58]. Structural confirmation of the functional moieties in both TPA-HATN-CMP and TPT-HATN-CMP was achieved using FTIR at room temperature [Fig. 2 (a)]. The spectra displayed prominent and nearly overlapping absorption bands. Noteworthy peaks appeared at 3041 and 1612 cm^{-1}, in agreement with C—H and C═N vibrations, respectively. Additionally, an evident signal at 1524 cm^{-1} confirmed the presence of aromatic C═C groups. In the ^{13}C NMR spectra [Fig. 2(b)], peaks observed between 150 and 120 ppm for TPA-HATN-CMP and TPT-HATN-CMP correspond to the aromatic rings present in their skeletal structures. Additionally, the peaks in the 164–169 ppm range are attributed to the phenazine units in both materials [64,65]. The thermal stability of electrode materials is a critical factor for their potential use in supercapacitor applications. To evaluate this, we analyzed the thermal stability of HATN-CMPs using thermogravimetric analysis (TGA) under N_2 [Fig. 2(c)]. Both TPA-HATN-CMP and TPT-HATN-CMP demonstrated remarkable thermal stability. The TPA-HATN-CMP showed T_{d10} at 633 °C and a char yield of 79%, while the TPT-HATN-CMP demonstrated a T_{d10} of 679 °C and a char yield of 78% [**Table S1**]. These results suggest that the TPT-HATN-CMP is more thermally robust. This enhanced stability can be attributed to the inclusion of the planar TPT moiety in the structure, which contributes to its improved thermal performance. In addition, the derivative thermogravimetric (DTG) profiles (**Fig. S4**) show that both HATN-CMPs exhibit two dominant mass-loss peaks at high temperatures, occurring at 556 and 758 °C for TPA-HATN-CMP and at 562 and 722 °C for TPT-HATN-CMP, which are indicative of decomposition governed by cleavage of the crosslinked backbone. As CMPs are typically amorphous in nature, powder X-ray diffraction (PXRD) analysis was carried out to investigate their structural characteristics. TPA-HATN and TPT-HATN-CMPs exhibited broad diffraction peaks in the range of (2θ =15–30°), confirming their amorphous nature [Fig. 2(d)]. The chemical composition of TPA-HATN-CMP and TPT-HATN-CMP, as revealed through X-ray photoelectron spectroscopy (XPS), revealed a notable presence of carbon (C) and nitrogen (N) elements [Fig. 2(e)], and XPS analysis showed nitrogen contents of 17.8% for TPA-HATN-CMP and 26.1% for TPT-HATN-CMP. The C 1 s spectra of TPA-HATN-CMP and TPT-HATN-CMP were deconvoluted to identify two distinct peaks corresponding to C═C/C═N and C—N bonding configurations [**Figs. S5(a) and S5(b)**]. Furthermore, two peaks observed in the N 1 s spectra of TPA-HATN-CMP and TPT-HATN-CMP verified the existence of N═C and N—C bonds [**Figs. S5(c) and S5(d)**]. Introducing nitrogen functionalities enhances electrochemical performance by facilitating pseudocapacitive processes,

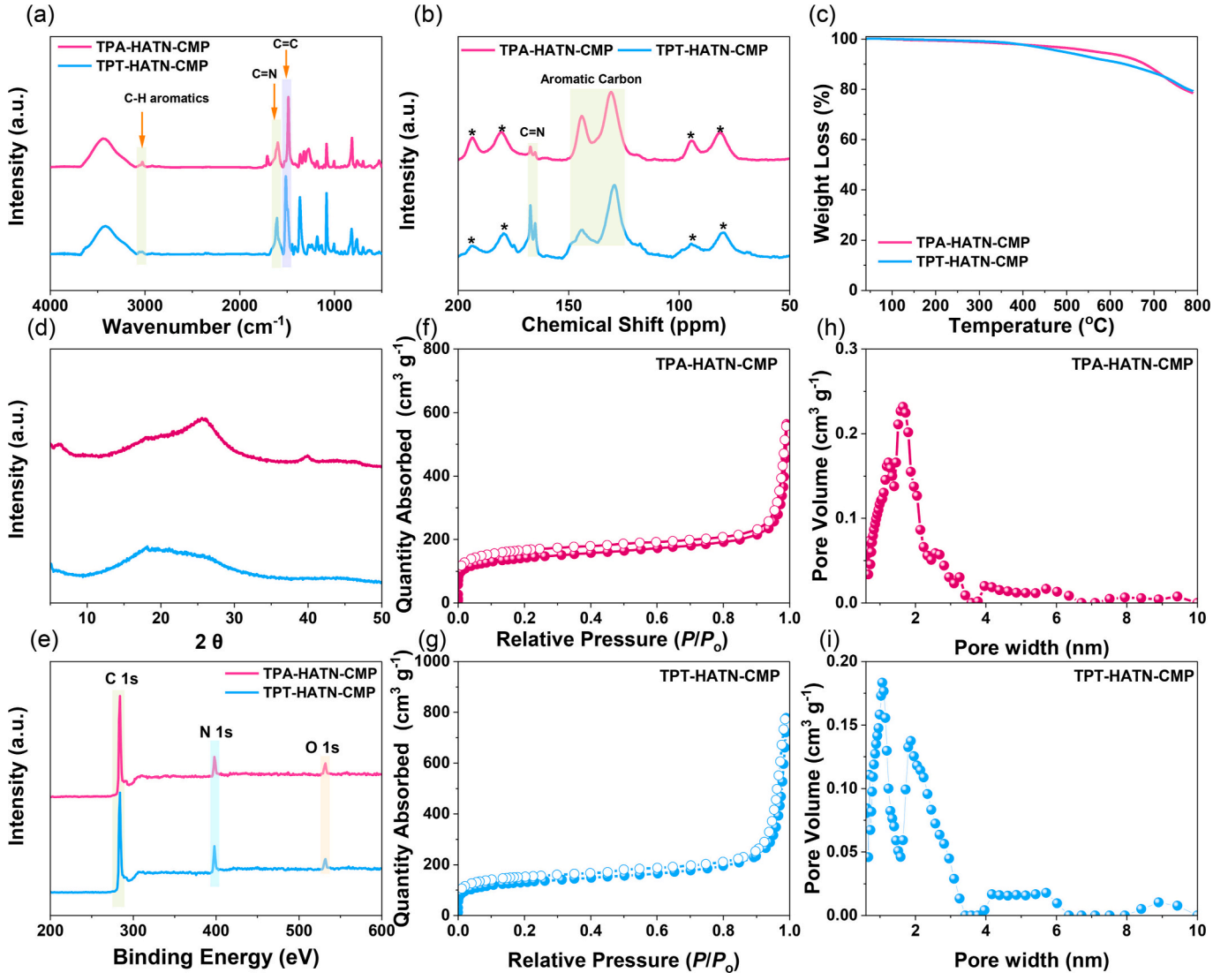

Fig. 2. (a) FTIR, (b) solid state ^{13}C NMR, (c) TGA, (d) XRD, and (e) XPS profiles of TPA-HATN-CMP and TPT-HATN-CMP. (f, g) N_2 adsorption/desorption profiles and (h, i) pore size diameters of (f, h) TPA-HATN-CMP and (g, i) TPT-HATN-CMP.

which results in increased capacitance upon interaction with the electrolyte [57,58].

To analyze the porous structure of our TPA-HATN-CMP and TPT-HATN-CMP, we conducted N_2 adsorption/desorption isotherm measurements [Figs. 2(f) and 2(g)]. Both TPA-HATN-CMP and TPT-HATN-CMP displayed type-II isotherms, characterized by a sharp increase in N_2 adsorption at P/P_0 values below 0.1 and a gradual rise at P/P_0 values above 0.97. This behavior indicates the presence of both meso- and micropores within the structures of these two HATN-CMPs. The pore size profile for TPA-HATN-CMP revealed two distinct, narrow peaks at 1.58 nm and 1.73 nm, whereas TPT-HATN-CMP exhibited a single, broader peak spanning 1.14 nm, confirming the porous nature of TPA-HATN and TPT-HATN-CMPs [Figs. 2(h) and 2(i) **and Table S1**]. Additionally, the pore volumes of TPA-HATN-CMP and TPT-HATN-CMP were measured at approximately 0.85 and 1.24 $cm^3\ g^{-1}$, respectively [**Table S1**]. The N_2 isotherms further indicated that TPA-HATN-CMP had a S_{BET} of 459 $m^2\ g^{-1}$, while TPT-HATN-CMP had 428 $m^2\ g^{-1}$ [**Table S1**]. These observations align with the pore-size distributions: TPT-HATN-CMP, with its larger pore volume, showed a lower BET surface area, whereas TPA-HATN-CMP, with smaller pores, showed a higher BET surface area. This inverse relationship between pore size and surface area is consistent with established principles of porous material characterization. Furthermore, TEM images highlighted the porous nature and lack of long-range order of the HATN-CMPs [**Figs. S5(e–h)**], which correlated well with the BET surface area and PXRD measurements. The high porosity observed in both HATN-CMPs is advantageous for ion transport and electrolyte accessibility, making them suitable for energy storage applications. The morphology of TPA-HATN-CMP and TPT-HATN-CMP was scrutinized using high-resolution scanning electron microscopy (SEM) along with SEM-EDS analysis [**Fig. S6**]. The SEM micrographs clearly displayed that both HATN-CMPs are composed of densely packed, aggregated nanoparticles with predominantly spherical morphologies, suggesting uniform growth during the polymerization process [**Figs. S6(a) and S6(d)**]. This aggregation is likely associated with π–π stacking, which promotes nanoparticle clustering. Elemental mapping from SEM-EDX confirmed the distribution of heteroatoms (C and N) throughout TPA-HATN and TPT-HATN-CMPs [**Figs. S6(b), S6(c), S6(e), and S6(f)**].

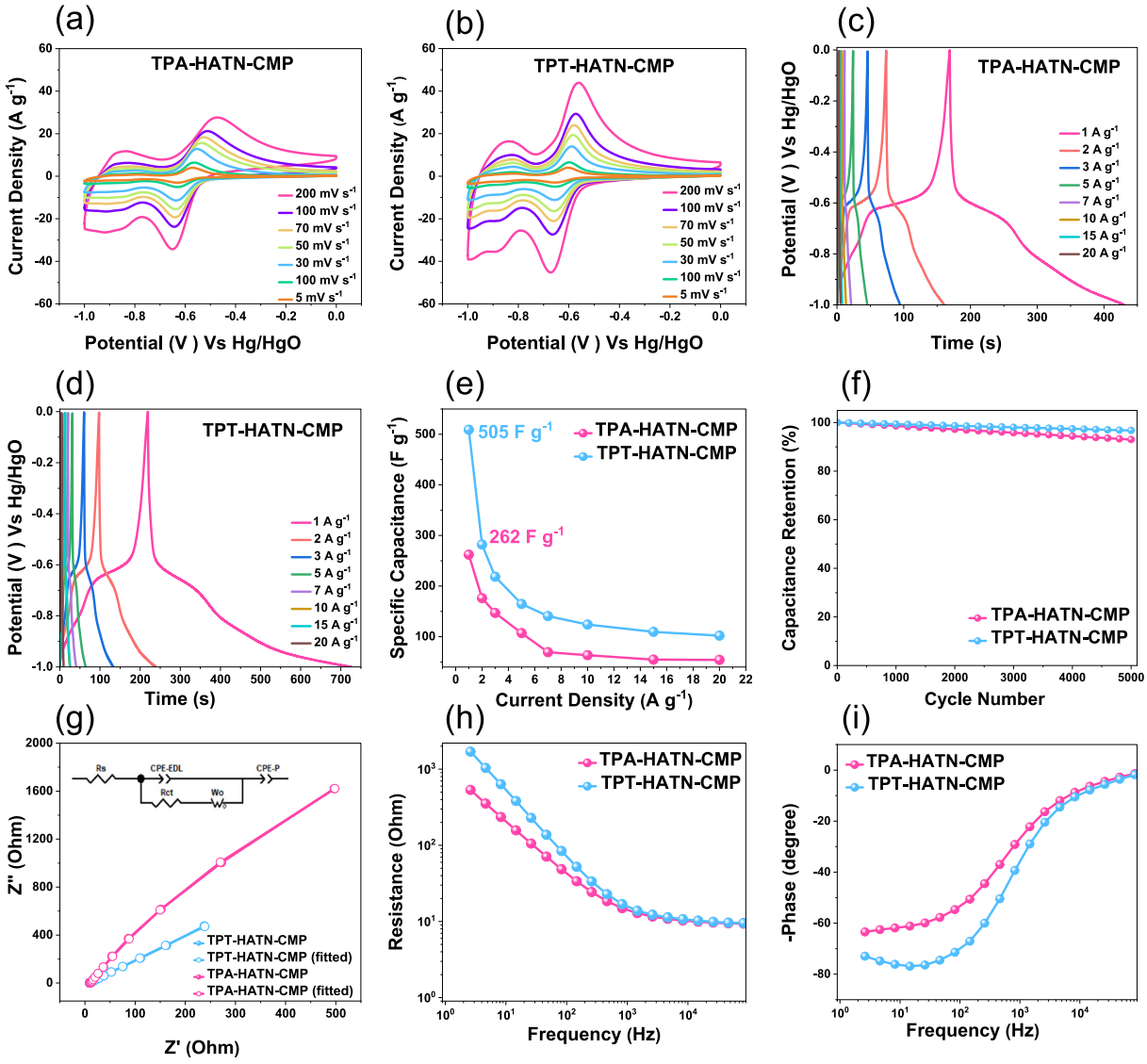

Fig. 3. (a, b) CV curves, (c, d) GCD curves, (e) specific capacitance, (f) capacitance retention, (g) EIS spectra, (h) Bode magnitude plot as a function of frequency, and (i) Bode phase-angle plots as a function of frequency of TPA-HATN and TPT-HATN-CMPs.

3.2. Electrochemical performance in a three-electrode setup of TPA-HATN-CMP and TPT-HATN-CMP

The TPA-HATN-CMP and TPT-HATN-CMP exhibited micro- and mesoporous structures, redox-active properties, indicating their potential as electrode materials for supercapacitors. We fabricated three-electrode supercapacitors using HATN-based CMPs coated electrodes in a 1 M KOH electrolyte and Hg/HgO as a reference electrode. The cyclic voltammetry (CV) measurements were investigated within the voltage window spanning −1.0 to 0.0 V at scan rates varying from 5 to 200 mV s^{-1} [Figs. 3(a) and 3(b)]. The CV plots revealed quasi-reversible redox behavior, confirming the pseudocapacitive characteristics of TPA-HATN-CMP and TPT-HATN-CMP [59]. At 5 mV s^{-1}, the reduction and oxidation peaks for TPA-HATN-CMP were manifested at −0.47 V and − 0.65 V, respectively, while for TPT-HATN-CMP, these peaks appeared at −0.54 V and − 0.67 V, respectively [Figs. 3(a) and 3(b)]. As the sweep rate was elevated from 5 to 200 mV s^{-1}, the oxidation profile shifted in a positive direction, and the reduction profile shifted in a negative direction. This resulted in a widening gap between the peak potentials, primarily due to the increased input impedance of the HATN-based CMPs coated electrodes [60,61]. Despite the increasing scan rates, the CV curves of both TPA-HATN-CMP and TPT-HATN-CMP maintained their shape, indicating high-rate performance and accelerated charge transfer kinetics [62]. The CV profiles show that the integrated area of TPT-HATN-CMP is significantly larger than that of TPA-HATN-CMP, indicating stronger faradaic contributions [Figs. 3(a) and 3(b)]. The observed differences in the CV integrated areas of the two HATN-CMPs can be primarily associated with variations in both nitrogen content and porosity within their polymeric frameworks. A higher concentration of nitrogen atoms introduces more redox-active sites, which actively participate in faradaic reactions and thereby enhance the overall pseudocapacitance. To better understand the origin of the redox features observed in the HATN-CMPs electrodes, CV profiles of the individual TPT-Br_3, TPA-Br_3, and HATN-Br_3 were measured at different current densities [**Fig. S7**]. The CV results indicate that TPT-Br_3 exhibits redox activity in the negative potential region [**Fig. S7(a)]** , whereas TPA-Br_3 shows only minor oxidation signals within the same range [**Fig. S7(b)]** . In contrast, HATN-Br_3 displays pronounced redox peaks between approximately −0.8 and − 0.4 V with substantially higher current responses [**Fig. S7(c)]** , confirming that the primary faradaic contributions in the CMPs arise predominantly from the electrochemically active HATN units. Galvanostatic charge–discharge (GCD) measurements were conducted at current densities ranging from 0.5 to 2 A g^{-1} to quantitatively assess the charge storage performance of the TPT-Br_3, TPA-Br_3, and HATN-Br_3 electrodes. The TPT-Br_3 and TPA-Br_3, electrodes exhibited symmetrical charge–discharge profiles [**Figs. S7(d)** and **S7(e)**]. In contrast, the HATN-Br_3 electrode displayed nonlinear charge–discharge behavior [**Fig. S7(f)**]. Based on the GCD profiles, the specific capacitance values of TPT-Br_3, TPA-Br_3, and HATN-Br_3 at a current density of 0.5 A g^{-1} were determined to be 36.2, 15.8, and 59.5 F g^{-1}, respectively [**Fig. S8**]. To obtain more accurate specific capacitance values, GCD analysis were recorded on HATN-based CMPs within the identical voltage range, employing current densities spanning 1 to 20 A g^{-1} [Figs. 3(c) and 3(d)]. The GCD curves for both HATN-based CMPs exhibited an inverted V-shape with significant bends, demonstrating pseudocapacitive and EDLC behavior. The pseudocapacitive response can be attributed to Faradaic charge-transfer processes between electrolyte ions and heteroatoms integrated within the microporous framework. The discharge duration was utilized alongside to calculate the specific capacitances [**Eq. S1**] of TPA-HATN-CMP and TPT-HATN-CMP. These were determined to be 262 and 505 F g^{-1} at 1 A g^{-1}, respectively [Fig. 3(e)]. The decline in specific capacitance at higher scan rates can be explained by the limited diffusion time for electrolyte ions to access the electrode surface [Fig. 3(e)]. The GCD measurements further demonstrated that the TPT-HATN-CMP exhibited a significantly longer discharge duration relative to the TPA-HATN-CMP electrode, indicating enhanced charge storage capability.

Prolonged cycling durability of TPA-HATN-CMP and TPT-HATN-CMP electrodes was evaluated at 10 A g^{-1} for 5000 charge–discharge cycles. Impressively, the electrodes retained 93% and 96.8% of their initial capacitance, respectively, indicating excellent electrochemical stability [Fig. 3(f)]. The CV and GCD results reveal that incorporation of redox-active HATN, TPA, and TPT into the framework notably impacts its redox behavior and energy storage capacity. Three-electrode supercapacitor configurations were fabricated using TPTPT-Br_3, TPA-Br_3, and HATN-Br_3 coated electrodes in a 1 M KOH electrolyte, with Ag/AgCl serving as the reference electrode. As shown in **Fig. S9(a-f)**, CV and GCD profiles of TPTPT-Br_3, TPA-Br_3, and HATN-Br_3 exhibited trends consistent with those observed in measurements conducted using Hg/HgO as the reference electrode, indicating good reproducibility of the electrochemical behavior across different reference systems. At 0.5 A g^{-1}, the specific capacitances of TPT-Br_3, TPA-Br_3, and HATN-Br_3 were measured to be 30.6, 13.3, and 46.6 F g^{-1}, respectively, as shown in **Fig. S10**. CV measurements of TPA-HATN-CMP and TPT-HATN-CMP, recorded within a potential window of −1.0 to 0.0 V at scan rates ranging from 5 to 200 mV s^{-1}, revealed quasi-reversible redox features, confirming the pseudocapacitive nature of both materials [**Fig. S11(a)** and **S11(b)**]. Furthermore, the GCD profiles of both HATN-based CMPs displayed inverted, nonlinear shapes with pronounced curvature, indicating the coexistence of pseudocapacitive and EDLC contributions [**Fig. S11(c)** and **S11(d)**]. The specific capacitances of TPA-HATN-CMP and TPT-HATN-CMP at a 1 A g^{-1} were determined to be 77.3 and 158 F g^{-1}, respectively [**Fig. S12**]. The variations in electrochemical behavior of TPA-HATN-CMP and TPT-HATN-CMP can be predominantly attributed to differences in nitrogen density. The increased nitrogen incorporation intrinsically improves electron-donating characteristics, surface polarity, and electrolyte wettability, all of which are favorable for charge storage. From a structure–activity perspective, the enhanced electrochemical performance arises from the synergistic effects of extended π-conjugated pathways that promote efficient electron transport and redox-active nitrogen-rich sites that introduce additional electrochemically active centers and enable reversible faradaic reactions. The elevated nitrogen content in TPT-HATN-CMP promotes more extensive redox activity, thereby contributing to higher capacitance [66–68]. Furthermore, the presence of the 1,3,5-triazine unit strengthens π-π stacking interactions, which facilitate improved electrolyte ion transport. The high degree of topological similarity between the two frameworks ensures that the observed performance differences originate mainly from nitrogen content rather than disparities in morphology or porosity. Although the TPA-based CMP exhibits a higher specific surface area, the superior supercapacitive performance of the TPT-based CMP is dominated by its higher nitrogen content. The increased density of nitrogen sites provides more redox-active centers and strengthens electrolyte–framework interactions, outweighing the contribution of surface area alone. **Table S2** presents a comparative overview of the specific capacitance values of HATN-CMPs, demonstrating that they surpass the performance of many previously reported electrode materials. In addition, **Table S2** reveals that TPT-HATN-CMP outperforms other organic CMP electrodes in terms of specific capacitance due to its higher nitrogen content, which provides additional redox-active centers. The presence of triazine moieties strengthens π–π stacking and facilitates ion diffusion, thereby enhancing overall electrochemical behavior [61]. Electrochemical impedance spectroscopy (EIS) was adopted to further understand the behavior of the HATN-CMPs [Fig. 3(g)]. After fitting the EIS data, the series resistances for TPA-HATN-CMP and TPT-HATN-CMP were assessed to be 9.13 Ω and 8.41 Ω, respectively. Notably, TPT-HATN-CMP exhibited lower resistance, highlighting its favorable characteristics for electrode applications. The Bode magnitude plot confirms the excellent capacitive nature of both materials in energy storage systems [Fig. 3(h)]. Moreover, the Bode phase-angle plots depict the knee frequencies of HATN-CMPs, which reflect their dynamic response characteristics. The knee point, identified

upon reaching a phase angle of 45° marks a transition between resistive and capacitive dominance. These values were found to be 627.12 Hz for TPA-HATN-CMP and 240.6 Hz for TPT-HATN-CMP [Fig. 3(i)]. The electric charge storage mechanism is schematically presented in Fig. 4. In this process, each HATN moiety functions as a redox-active site, capable of accepting six electrons during charging [57]. Meanwhile, the TPT segment undergoes a two-electron reduction, forming the TPT^{2-} species [6,69]. These synergistic redox processes endow TPT-HATN-CMP with pronounced electrochemical activity. Owing to TPT-HATN-CMP having a relatively lower surface area than TPA-HATN-CMP, the material primarily exhibits redox-governed behavior rather than relying on electric double-layer capacitance. As shown in Figs. 4(a) and 4(b), both HATN and TPT units experience reduction during discharge and are re-oxidized in the subsequent charging phase, with TPT^{2-} and $HATN^{6-}$ species reverting to their neutral states. The redox reactions of HATN and TPT occur cooperatively, likely through π–π stacking interactions, which is supported by the presence of redox peaks at −0.54 and − 0.67 V in the CV plot [Figs. 4(a) and 4(b)]. During the charging sequence, the extended conjugation within the HATN and TPT framework enhances electron mobility, ensuring efficient energy storage. Whereas the discharge process releases stored charge, restoring the original structure [Fig. 4(c)]. This reversible redox behavior significantly enhances electrochemical properties, positioning TPT-HATN-CMP as a viable electrode material for energy storage systems.

The structural stability of the TPA-HATN-CMP and TPT-HATN-CMP electrodes after electrochemical evaluation was investigated using SEM and XPS analyses. SEM images obtained after cycling reveal that both HATN-CMPs electrodes maintain a morphology composed of closely aggregated nanoparticles with predominantly spherical features, comparable to their pristine state [**Fig. S13**]. Furthermore, XPS analysis confirms the presence of all constituent elements along with their corresponding core-level spectra after cycling, indicating stable surface chemistry without detectable degradation or elemental loss [**Fig. S14**]. Collectively, these results demonstrate the excellent structural and chemical robustness of the HATN-CMPs electrodes, which is consistent with their high cycling stability and sustained electrochemical performance. The prominent enclosed area and highly reversible redox peaks indicate that energy storage in HATN-CMPs electrodes arises from a

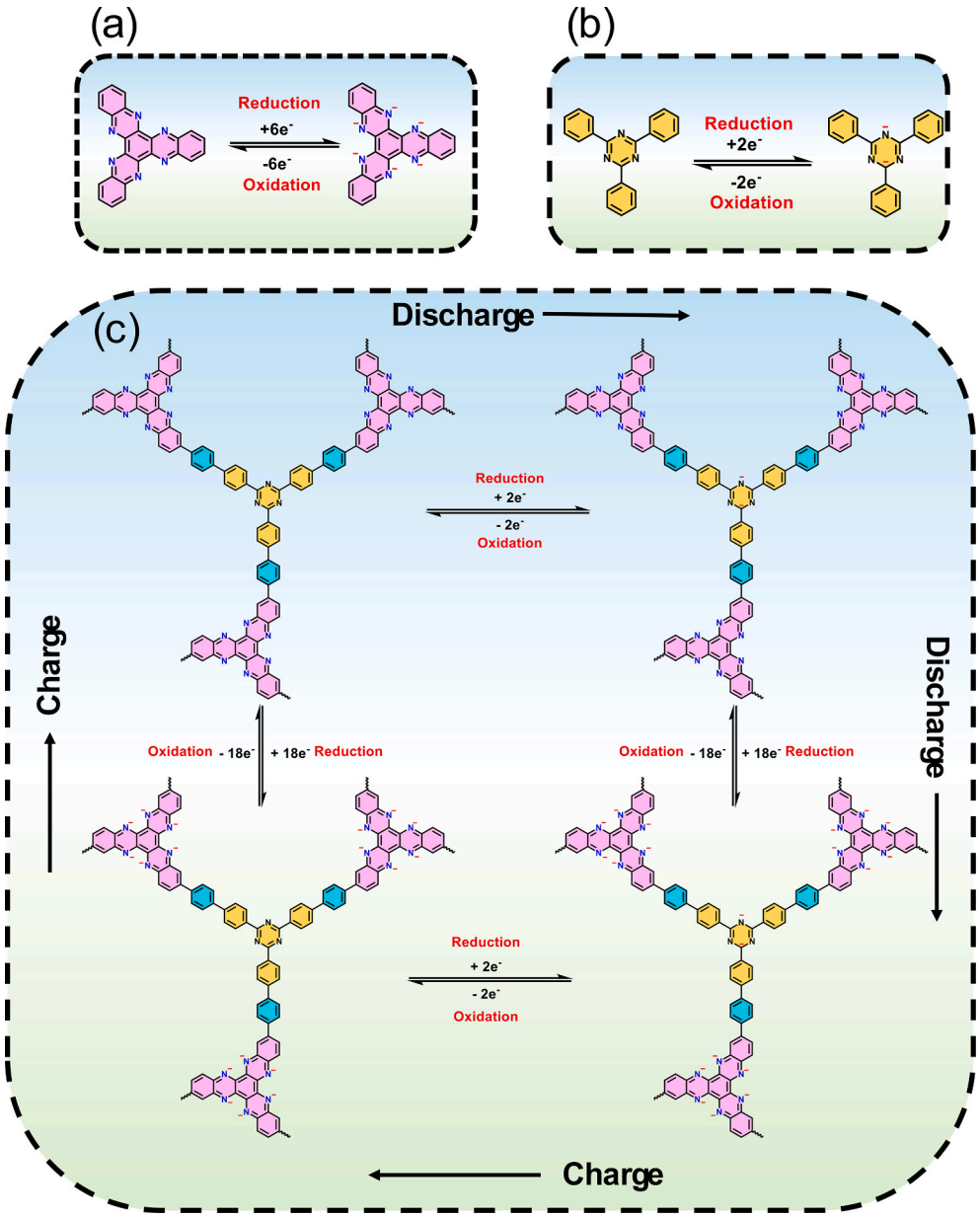

Fig. 4. The possible charging-discharging mechanism of (a) HATN, (b)TPT, and (c) TPT-HATN-CMP.

synergistic combination of EDLC and faradaic processes. To quantitatively deconvolute these contributions, the Trasatti analysis was employed, with full computational details provided in the **ESI**. Areal capacitances were calculated across scan rates from 5 to 200 mV s^{-1} using the established methodology (**ESI**). A linear fit is obtained by illustrating the inverse areal capacitance (C^{-1}) and the (scan rate, $v^{1/2}$), characteristic of diffusion of ions in a semi-infinite domain, where the intercept represents the inverse of the total capacitance [Fig. 5(a)]. Conversely, illustrating areal capacitance (C) versus the inverse (scan rate, $v^{1/2}$) under the same diffusion assumption yields a linear fit whose intercept quantifies the EDLC contribution [Fig. 5(b)]. These analyses provide a detailed partitioning of pseudocapacitive versus EDLC contributions for TPA-HATN-CMP and TPT-HATN-CMP, respectively [Figs. 5(c) and 5(d)], highlighting the interplay between surface adsorption and diffusion-controlled faradaic mechanisms in determining the overall capacitance performance. At 5 mV s^{-1}, the TPA-HATN-CMP exhibited a capacitive contribution of 39% and a diffusion-controlled contribution of 61% [Fig. 5(e)], whereas TPT-HATN-CMP displayed a lower capacitive fraction of 29% and a higher diffusion-controlled contribution of 71% [Fig. 5(f)]. This difference suggests that TPT-HATN-CMP has a more pronounced reliance on ion diffusion, likely due to a higher density of redox-active nitrogen sites, which facilitates faradaic charge storage. These distinctions underscore how structural features and ion transport kinetics collectively influence the balance between capacitive and diffusion-controlled processes in CMP electrodes.

3.3. *Electrochemical performance in a two-electrode setup of TPT-HATN-CMP*

Based on the promising electrochemical results obtained from the three-electrode measurements, it was confirmed that TPT-HATN-CMP exhibits excellent specific capacitance, making it a highly suitable candidate for energy storage applications. To evaluate its practical

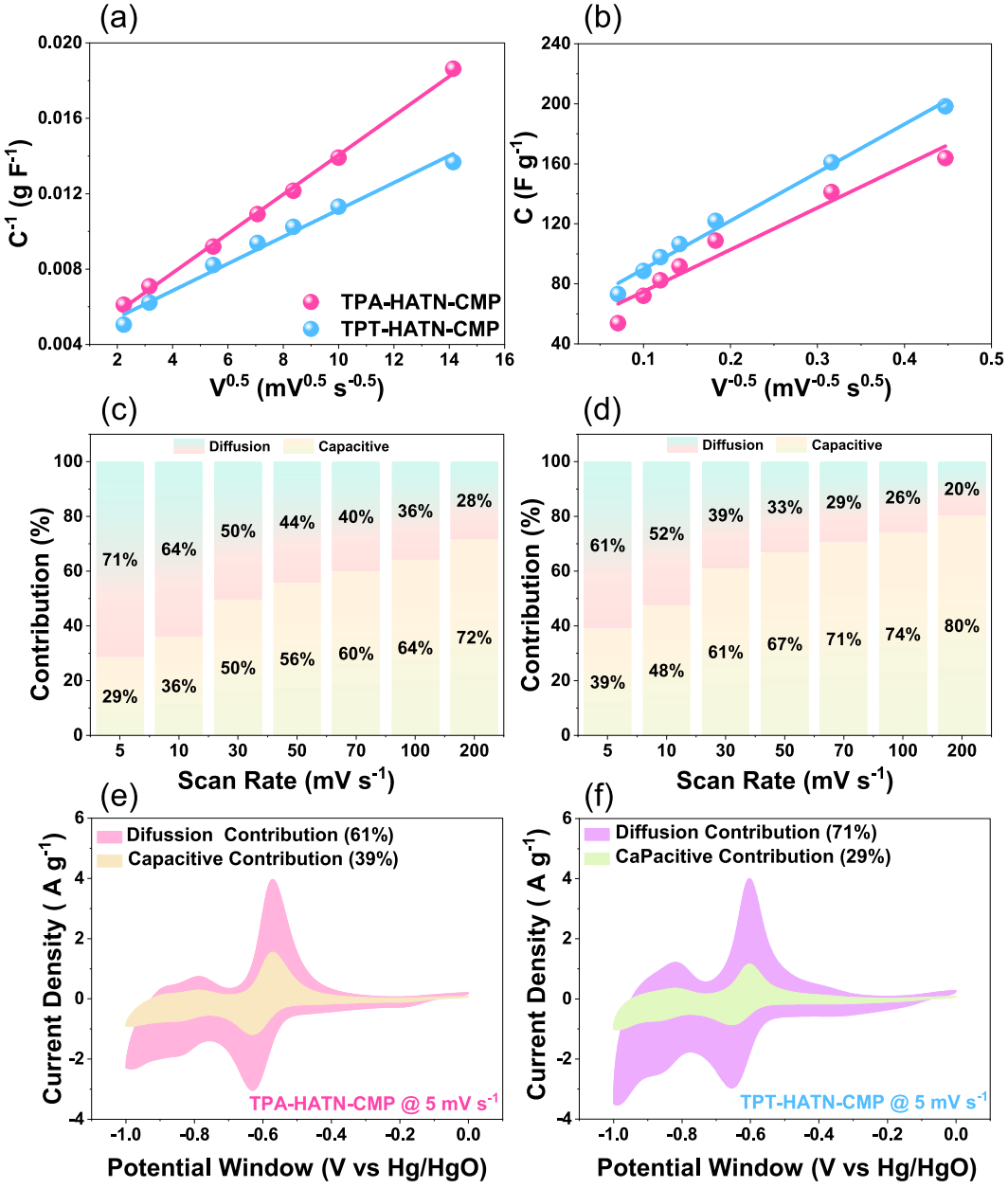

Fig. 5. (a) Graphs of inverse areal capacitance (C^{-1}) vs (scan rate, $v^{1/2}$), (b) Graphs of gravimetric capacitance vs (the inverse scan rate, $v^{-1/2}$), the percentage capacitance contribution of (c) TPA-HATN-CMP, (d) TPT-HATN-CMP, and the capacitive and diffusion at 5 mV s^{-1} (e) TPA-HATN-CMP and (f) TPT-HATN-CMP.

performance, a symmetric supercapacitor coin cell (CR-2032) was fabricated using 1 M KOH as the electrolyte, with TPT-HATN-CMP employed as both the negative and positive electrode [Fig. 6(a)]. The obtained CV curves display a nearly rectangular shape with distinct humps, revealing the presence of both EDLC and pseudocapacitive contributions [Fig. 6(b)]. With increasing scan rates, the current response also increases, demonstrating the excellent rate performance and structural stability of the TPT-HATN-CMP electrode, which are essential attributes for supercapacitor applications. The charge–discharge curves revealed a nearly triangular configuration, signifying a combination of EDLC and pseudocapacitive contributions [Fig. 6(c)]. The specific capacitance values of symmetric TPT-HATN-CMP device, calculated using **eq. S2**, were found to be 219.4, 191.24, 169.3, 143.05, 117.6, and 94.35 F g^{-1} at 1, 2, 3, 5, 7, and 10 A g^{-1}, respectively [Fig. 6(d)]. These results demonstrate the reliable electrochemical performance of the fabricated supercapacitor device. The Ragone plot of the symmetric supercapacitor fabricated using TPT-HATN-CMP reveals an outstanding energy density of 22.01 Wh kg^{-1}, which was achieved at an operating voltage of 0.85 V, along with a power density of 846 W kg^{-1}. [Fig. 6(e)]. These values highlight the ability of TPT-HATN-CMP to achieve superior energy storage and rapid charge–discharge capability, making it highly competitive with many reported redox-active supercapacitors. This balance between energy and power density demonstrates the practical potential of TPT-HATN-CMP toward high-performance storing of electrical energy, underscoring the advantages of incorporating TPT and HATN units into CMPs, offering several important advantages for supercapacitor applications. Furthermore, the cycling stability of the symmetric TPT-HATN-CMP device was examined at 10 A g^{-1} for 5000 charge–discharge cycles [Fig. 6(f)]. The electrode maintained 80.8% of its original capacitance, confirming its high stability and structural robustness.

To gain deeper insight into the electrochemical behavior of both TPA-HATN and TPT-HATN CMPs, we performed density functional theory (DFT) calculations on both CMPs to elucidate their optimized geometrical structures and electronic characteristics. The frontier molecular orbitals (HOMO and LUMO) and corresponding energy levels were computed at the B3LYP-D3(BJ)/6-31G(d) level of theory. **Fig. S15** presents the HOMO–LUMO isosurface maps of TPA-HATN and TPT-HATN CMPs. In TPA-HATN and TPT-HATN, the LUMO is primarily delocalized over the HATN core. This seven-ring system is planar and highly conjugated, enhancing its electronic accepting ability and thereby stabilizing the LUMO. The calculated LUMO energies are −2.60 eV for TPA-HATN CMP and − 2.66 eV for TPT-HATN CMP, indicating that TPT-HATN possesses a slightly stronger electron-withdrawing character. The HOMO distributions differ between the two CMPs. In TPA-HATN CMP, the HOMO is mainly localized on the TPA unit, where the phenyl rings exhibit a torsional angle of approximately 34.8°, limiting π-conjugation across the framework. Conversely, in TPT-HATN CMP, the HOMO extends over the connected phenyl units, suggesting improved conjugation. The calculated HOMO–LUMO gaps are 2.37 eV for TPA-HATN CMP and 3.29 eV for TPT-HATN CMP. These results imply that TPT-HATN CMP is a slightly better electron acceptor. To further elucidate the electronic characteristics of TPA-HATN and TPT-HATN CMPs, the molecular electrostatic surface potentials (MESPs) were computed to predict the electroactive regions within each molecule, as depicted in **Fig. S16**. The MESP maps reveal several electron-rich regions, represented by red areas, which correspond to sites with high nucleophilicity and potential redox activity. The regions of highest electron density—highlighted in deep red—are localized around the nitrogen atoms of the HATN core, exhibiting negative electrostatic potentials (ESPs) of −49 kcal mol^{-1} for TPA-HATN CMP and − 48 kcal mol^{-1} for TPT-HATN CMP. These zones are the most favorable for electrophilic attack and are likely to participate in redox processes. A secondary negatively charged region is observed around the nitrogen atoms of the TPT unit, with ESP values of approximately −18 kcal mol^{-1}, also contributing to the electrochemical activity through proton

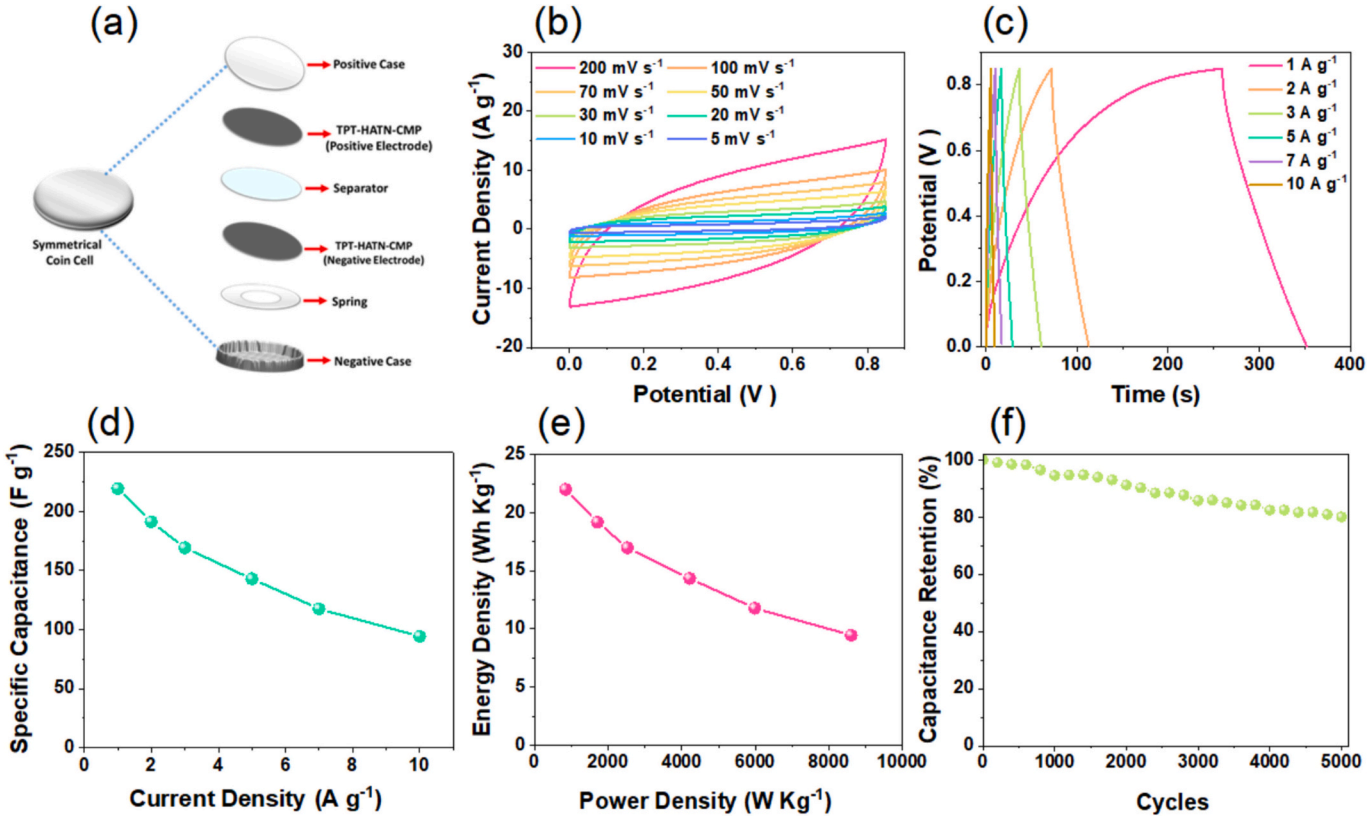

Fig. 6. (a) Fabrication of TPT-HATN-CMP symmetric coin cell, (b) CV profiles, (c) GCD profiles, (d) specific capacitance, (e) Ragone plot, and (f) capacitance retention of TPT-HATN-CMP.

adsorption. In contrast, the most electrophilic regions are associated with the terminal hydrogen atoms, displaying positive ESP values in the range of 16–17 kcal mol^{-1}. Overall, the MESP analysis provides a clear visualization of the reactive centers in both HATN-CMPs, indicating that the nitrogen atoms within the conjugated framework play a key role in governing their electrochemical behavior.

4. Conclusion

We successfully synthesized two redox-active porous materials (TPA-HATN-CMP and TPT-HATN-CMP) through a Suzuki coupling reaction, having high thermal stability and BET surface area. The potential application of these CMPs in supercapacitors was thoroughly investigated. Both materials demonstrated excellent conductivity, efficient faradaic energy storage, and rapid charge transfer capabilities. Notably, the TPT-HATN-CMP exhibited a specific capacitance of 505 F g^{-1} at 1 A g^{-1}, exceptional stability, retaining 96.8% of their capacitance after 5000 charge-discharge cycles in a three-electrode system. In a symmetric two-electrode setup, the TPT-HATN-CMP displayed a capacitance of 219.4 F g^{-1} and an energy density of 22.01 Wh kg^{-1} at a power density of 846 W kg^{-1}. After 5000 cycles, the symmetric TPT-HATN-CMP device maintained 80.8% of its initial capacitance. These findings highlight the potential of HATN-CMPs as high-performance redox materials for use in conductive devices, batteries, and advanced energy storage systems. This research leads to the rational design of efficient CMPs for next-generation energy storage technologies.

CRediT authorship contribution statement

Mohamed Gamal Mohamed: Writing – review & editing, Writing – original draft, Supervision, Methodology, Investigation, Formal analysis, Data curation, Conceptualization. **Mohsin Ejaz:** Writing – review & editing, Writing – original draft, Data curation, Conceptualization. **Abdul Basit:** Formal analysis. **Yang-Chin Kao:** Formal analysis. **Ahmed A.K. Mohammed:** Software. **Shiao-Wei Kuo:** Supervision, Resources, Project administration.

Declaration of competing interest

The authors declare that they have no known competing financial interests or personal relationships that could have appeared to influence the work reported in this paper.

Acknowledgments

This study was supported financially by the National Science and Technology Council, Taiwan, under contracts NSTC 114-2223-E-110-001- and 113-2221-E-110-012-MY3. The authors thank the staff at National Sun Yat-sen University for their assistance with the TEM (ID: EM022600) experiments.

Appendix A. Supplementary data

Supplementary data to this article can be found online at https://doi.org/10.1016/j.est.2026.121329.

Data availability

Data will be made available on request.

References

[1] J. Min, G. Yan, A.M. Abed, S. Elattar, M.A. Khadimallah, A. Jan, H.E. Ali, The effect of carbon dioxide emissions on the building energy efficiency, Fuel 326 (2022) 124842, https://doi.org/10.1016/j.fuel.2022.124842.

[2] M.D. Ahmed, K.M. Maraz, Revolutionizing energy storage: Overcoming challenges and unleashing the potential of next generation lithium-ion battery technology, Mater. Eng. Res. 5 (2023) 265–278, https://doi.org/10.25082/MER.2023.01.003.

[3] A. Basit, M.G. Mohamed, H. Karim, S.W. Kuo, Synergistic engineering of Anthracene and Thiazolo[5,4-d] thiazole–based donor–acceptor conjugated microporous polymers with heteroatom adoption for enhanced energy storage capacity, J. Mater. Chem. A 13 (2025) 41913–41930, https://doi.org/10.1039/D5TA05442G.

[4] M. Ejaz, M.G. Mohamed, W.C. Chang, S.W. Kuo, Synthesis and design of hypercrosslinked porous organic frameworks containing tetraphenylpyrazine unit for high-performance supercapacitor, J. Polym. Sci. 62 (2024) 1629–1638, https://doi.org/10.1002/pol.20230174.

[5] A. Basit, Y.C. Kao, Y.A. El-Ossaily, S.W. Kuo, M.G. Mohamed, Rational engineering and synthesis of pyrene and thiazolo [5, 4-d] thiazole-functionalized conjugated microporous polymers for efficient supercapacitor energy storage, J. Mater. Chem. A 12 (2024) 30508–30521, https://doi.org/10.1039/D4TA05908E.

[6] S.V. Chaganti, S.U. Sharma, M. Ibrahim, A. Basit, P.N. Singh, S.W. Kuo, M. G. Mohamed, Redox-active a pyrene-4,5,9,10-tetraone and thienyltriazine-based conjugated microporous polymers for boosting faradaic supercapacitor energy storage, J. Power Sources 627 (2025) 235848, https://doi.org/10.1016/j.jpowsour.2024.235848.

[7] M. Ejaz, M.G. Mohamed, Y.T. Chen, K. Zhang, S.W. Kuo, Porous carbon materials augmented with heteroatoms derived from hyperbranched biobased benzoxazine resins for enhanced CO_2 adsorption and exceptional supercapacitor performance, J. Energy Storage 78 (2024) 110166, https://doi.org/10.1016/j.est.2023.110166.

[8] L. Phor, A. Kumar, S. Chahal, Electrode materials for supercapacitors: A comprehensive review of advancements and performance, J. Energy Storage 84 (2024) 110698, https://doi.org/10.1016/j.est.2024.110698.

[9] E. Dhandapani, S. Thangarasu, S. Ramesh, K. Ramesh, R. Vasudevan, N. Duraisamy, Recent development and prospective of carbonaceous material, conducting polymer and their composite electrode materials for supercapacitor a review, J. Energy Storage 52 (2022) 104937, https://doi.org/10.1016/j.est.2022.104937.

[10] L. Hao, X. Li, L. Zhi, Carbonaceous electrode materials for supercapacitors, Adv. Mater. 25 (2013) 3899–3904, https://doi.org/10.1002/adma.201301204.

[11] X. Hu, G. Zhang, H. Liang, J. Li, H. Zhou, L.H. Chung, J. He, An oxazole-linked donor–acceptor covalent organic framework as an efficient electrocatalyst for lithium–sulfur batteries, J. Mater. Chem. A 13 (2025) 3392–3401, https://doi.org/10.1039/D4TA07994A.

[12] X. Hu, Z. Lin, S. Wang, G. Zhang, S. Lin, T. Huang, R. Chen, L.H. Chung, J. He, Highly crystalline flower-like covalent-organic frameworks enable highly stable zinc metal anodes, ACS Appl. Energy Mater. 5 (2022) 3715–3723, https://doi.org/10.1021/acsaem.2c00154.

[13] J. Park, D. Kim, S. Kim, J. Park, D.Y. Ryu, J. Kim, H. An, J. Kim, Controlled growth of redox-active polymer nanorods on MOF-derived activated nanoporous carbons: 3D reconstruction study and high-performance supercapacitor, Chem. Eng. J. 498 (2024) 155122, https://doi.org/10.1016/j.cej.2024.155122.

[14] S.U. Sharma, M.H. Elsayed, I.M.A. Mekhemer, T.S. Meng, H.H. Chou, S.W. Kuo, M. G. Mohamed, Rational design of pyrene and thienyltriazine-based conjugated microporous polymers for high-performance energy storage and visible-light photocatalytic hydrogen evolution from water, Giant 17 (2024) 100217, https://doi.org/10.1016/j.giant.2023.100217.

[15] G. Zhang, L. Deng, J. Liu, J. Zhang, J. Wang, W. Li, X. Li, Controllable intercalated polyaniline nanofibers highly enhancing the utilization of delaminated RuO_2 nanosheets for high-performance hybrid supercapacitors, ChemElectroChem 9 (2022) e202200039, https://doi.org/10.1002/celc.202200039.

[16] S. Peng, L. Li, H. Tan, R. Cai, W. Shi, C. Li, S.G. Mhaisalkar, M. Srinivasan, S. Ramakrishna, Q. Yan, MS 2 (M = co and Ni) hollow spheres with tunable interiors for high-performance supercapacitors and photovoltaics, Adv. Funct. Mater. 24 (2014) 2155–2162, https://doi.org/10.1002/adfm.201303273.

[17] X. Zhang, H. Li, W. Zhang, Z. Huang, C.P. Tsui, C. Lu, C. He, Y. Yang, In-situ growth of polypyrrole onto bamboo cellulose-derived compressible carbon aerogels for high performance supercapacitors, Electrochim. Acta 301 (2019) 55–62, https://doi.org/10.1016/j.electacta.2019.01.166.

[18] Y. Xu, Y. Tao, X. Zheng, H. Ma, J. Luo, F. Kang, Q.H. Yang, A metal-free supercapacitor electrode material with a record high volumetric capacitance over 800 F cm, Adv. Mater. 27 (2015) 8082–8087, https://doi.org/10.1002/adma.201504151.

[19] K. Jayaramulu, D.P. Dubal, B. Nagar, V. Ranc, O. Tomanec, M. Petr, K. Kumara, R. Datta, R. Zboril, P. Gómez-Romero, R.A. Fischer, Ultrathin hierarchical porous carbon nanosheets for high-performance supercapacitors and redox electrolyte energy storage, Adv. Mater. 30 (2018) 1705789, https://doi.org/10.1002/adma.201705789.

[20] M. Ejaz, M.G. Mohamed, S.W. Kuo, Solid state chemical transformation provides a fully benzoxazine-linked porous organic polymer displaying enhanced CO_2 capture and supercapacitor performance, Polym. Chem. 14 (2023) 2494–2509, https://doi.org/10.1039/D3PY00158J.

[21] M. Ejaz, M.G. Mohamed, W.-C. Huang, S.-W. Kuo, Pyrene-based covalent organic polymers with nano carbonaceous composites for efficient supercapacitive energy storage, J. Mater. Chem. A 11 (2023) 22868–22883, https://doi.org/10.1039/D3TA02741D.

[22] M. Ejaz, M.M. Samy, Y. Ye, S.-W. Kuo, M.G. Mohamed, Design hybrid porous organic/inorganic polymers containing polyhedral oligomeric Silsesquioxane/pyrene/anthracene moieties as a high-performance electrode for supercapacitor, Int. J. Mol. Sci. 24 (2023) 2501, https://doi.org/10.3390/ijms24032501.

[23] M. Ejaz, M.G. Mohamed, S.U. Sharma, J.-T. Lee, C.-F. Huang, T. Chen, S.W. Kuo, An Ultrastable porous polyhedral oligomeric Silsesquioxane/Tetraphenylthiophene hybrid as a high-performance electrode for supercapacitors, Molecules 27 (2022) 6238, https://doi.org/10.3390/molecules27196238.
[24] M. Ejaz, M.G. Mohamed, S.-W. Kuo, Fluorescent benzoxazine–perylene linked covalent organic polymer as a sensing probe for lead ions and 2,4,6-trinitrophenol, ACS Appl. Polym. Mater. 6 (2024) 9170–9179, https://doi.org/10.1021/acsapm.4c01514.
[25] C. Li, H. Xu, H. Xiong, S. Xia, X. Peng, F. Xu, X. Chen, Π-bridge modulations in D–π–a conjugated microporous polymers to facilitate charge separation and transfer kinetics for efficient Photocatalysis, Adv. Funct. Mater. 34 (2024) 2405539, https://doi.org/10.1002/adfm.202405539.
[26] M.G. Mohamed, C.C. Chen, M. Ibrahim, A.O. Mousa, M.H. Elsayed, Y. Ye, S.W. Kuo, Tetraphenylanthraquinone and Dihydroxybenzene-tethered conjugated microporous polymer for enhanced CO_2 uptake and Supercapacitive energy storage, JACS Au 4 (2024) 3593–3605, https://doi.org/10.1021/jacsau.4c00537.
[27] M.G. Mohamed, M.H. Elsayed, C.J. Li, A.E. Hassan, I.A.M. Mekhemer, A.F. Musa, M.K. Hussien, L.C. Chen, K.H. Chen, H.H. Chou, S.W. Kuo, Reticular design and alkyne bridge engineering in donor–π–acceptor type conjugated microporous polymers for boosting photocatalytic hydrogen evolution, J. Mater. Chem. A 12 (2024) 7693–7710, https://doi.org/10.1039/D3TA07309B.
[28] K. Amin, B.C. Baker, L. Pan, W. Mehmood, Z. Hao, R. Nawaz, Z. Wei, C.F.J. Faul, Triphenylamine-based conjugated microporous polymers as the next generation organic cathode materials, Adv. Mater. 37 (2025) 2410262, https://doi.org/10.1002/adma.202410262.
[29] J. Xu, R. Jiang, Z. Qiu, C. Chen, B. Liu, X. Hu, B. Wang, M. Zhang, L. Shen, H. Lin, Conjugated microporous polymer for membrane separation: A review, Sep. Purif. Technol. 362 (2025) 131795, https://doi.org/10.1016/j.seppur.2025.131795.
[30] L.F. Yang, Y.Z. Zhu, C.C. Zhang, J.Y. Zheng, Electron-donor engineering of Heptazine-based donor-acceptor conjugated microporous polymers for efficient metal-free photocatalytic hydrogen evolution, J. Mater. Chem. A 13 (2025) 14708–14715, https://doi.org/10.1039/D5TA01288K.
[31] A. Hayat, M. Sohail, A. El Jery, K.M. Al-Zaydi, S. Raza, H. Ali, Y. Al-Hadeethi, T. A. Taha, I.U. Din, M.A. Khan, M.A. Amin, Recent advances in ground-breaking conjugated microporous polymers-based materials, their synthesis, modification and potential applications, Mater. Today 64 (2023) 180–208, https://doi.org/10.1016/j.mattod.2023.02.025.
[32] N. Wan, Q. Chang, F. Hou, S. Zhang, X. Zang, X. Zhao, C. Wang, Z. Wang, Y. Yamauchi, Nanoarchitectured conjugated microporous polymers: State of the art synthetic strategies and opportunities for adsorption science, Chem. Mater. 34 (2022) 7598–7619, https://doi.org/10.1021/acs.chemmater.2c00999.
[33] W. He, J. Duan, H. Liu, C. Qian, M. Zhu, W. Zhang, Y. Liao, Conjugated microporous polymers for advanced chemical sensing applications, Prog. Polym. Sci. 148 (2024) 101770, https://doi.org/10.1016/j.progpolymsci.2023.101770.
[34] C. Han, S. Xiang, S. Jin, C. Zhang, J.X. Jiang, Rational design of conjugated microporous polymer photocatalysts with definite D– π–a structures for ultrahigh photocatalytic hydrogen evolution activity under natural sunlight, ACS Catal. 13 (2022) 204–212, https://doi.org/10.1021/acscatal.2c04993.
[35] M.G. Mohamed, S.V. Chaganti, S.U. Sharma, M.M. Samy, M. Ejaz, J.T. Lee, K. Zhang, S.W. Kuo, Constructing conjugated microporous polymers containing the Pyrene-4,5,9,10-Tetraone unit for energy storage, ACS Appl. Energy Mater. 5 (2022) 10130–10140, https://doi.org/10.1021/acsaem.2c01842.
[36] M.G. Mohamed, M. Ibrahim, N.P. Chen, A. Basit, Y.C. Kao, A.O. Mousa, M. M. Samy, S.W. Kuo, Tetrabenzonaphthalene and redox-active Anthraquinone-linked conjugated microporous polymers as organic electrodes for enhanced energy storage efficiency, ACS Appl. Energy Mater. 7 (2024) 5582–5593, https://doi.org/10.1021/acsaem.4c01276.
[37] M.G. Mohamed, S.V. Chaganti, M.S. Li, M.M. Samy, S.U. Sharma, J.T. Lee, M. H. Elsayed, H.H. Chou, S.W. Kuo, Ultrastable porous organic polymers containing Thianthrene and pyrene units as organic electrode materials for supercapacitors, ACS Appl. Energy Mater. 5 (2022) 6442–6452, https://doi.org/10.1021/acsaem.2c00942.
[38] M.G. Mohamed, B.X. Su, S.W. Kuo, Robust nitrogen-doped microporous carbon via crown ether-functionalized Benzoxazine-linked porous organic polymers for enhanced CO_2 adsorption and supercapacitor applications, ACS Appl. Mater. Interfaces 16 (2024) 340858–340872, https://doi.org/10.1021/acsami.4c05645.
[39] K. Amin, N. Ashraf, L. Mao, C.F.J. Faul, Z. Wei, Conjugated microporous polymers for energy storage: Recent progress and challenges, Nano Energy 85 (2021) 105958, https://doi.org/10.1016/j.nanoen.2021.105958.
[40] T. Huang, G. Zhang, R. Chen, S. Lin, H. Zhou, J. Li, L.H. Chung, X. Hu, L. Yu, J. He, Donor–acceptor conjugated microporous polymer toward enhanced redox kinetics in lithium–sulfur batteries, ACS Appl. Mater. Interfaces 15 (2023) 21075–21085, https://doi.org/10.1021/acsami.3c01558.
[41] A.M. Khattak, H. Sin, Z.A. Ghazi, X. He, B. Liang, N.A. Khan, H.R. Alanagh, A. Iqbal, L. Li, Z. Tang, Controllable fabrication of redox-active conjugated microporous polymers on reduced graphene oxide for high performance faradaic energy storage, J. Mater. Chem. A 6 (2018) 18827–18832, https://doi.org/10.1039/C8TA07913G.
[42] N. Meng, H. Li, Y. Liu, Y. Liao, Self-templating synthesis of nitrogen-rich porous carbons using pyridyl functionalized conjugated microporous polytriphenylamine for electrochemical energy storage, Electrochim. Acta 402 (2021) 139531, https://doi.org/10.1016/j.electacta.2021.139531.
[43] Y. Cho, M. Jang, K.S. Lee, E. Lee, S.Y. Park, Y. Piao, The quinone-based conjugated microporous polymer as an effective electrode additive for activated graphene host material in lithium-sulfur batteries, Chem. Eng. J. 463 (2023) 142422, https://doi.org/10.1016/j.cej.2023.142422.
[44] Y. Liao, H. Wang, M. Zhu, A. Thomas, Efficient supercapacitor energy storage using conjugated microporous polymer networks synthesized from buchwald–hartwig coupling, Adv. Mater. 30 (2018) 1705710, https://doi.org/10.1002/adma.201705710.
[45] M. Li, J. Liu, Y. Li, G. Xing, X. Yu, C. Peng, L. Chen, Skeleton engineering of isostructural 2d covalent organic frameworks: Orthoquinone redox-active sites enhanced energy storage, CCS Chem. 3 (2021) 696–706, https://doi.org/10.31635/ccschem.020.202000257.
[46] D.H. Roh, H. Shin, H.T. Kim, T.H. Kwon, Sono-cavitation and nebulization-based synthesis of conjugated microporous polymers for energy storage applications, ACS Appl. Mater. Interfaces 13 (2021) 61598–61609, https://doi.org/10.1021/acsami.1c13755.
[47] M. Zhang, T. Zhao, J. Dou, Z. Xu, W. Zhang, X. Chen, X. Wang, B. Zhou, Bottom-up construction of conjugated microporous polyporphyrin-coated graphene hydrogel composites with hierarchical pores for high-performance capacitors, ChemElectroChem 6 (2019) 5946–5950, https://doi.org/10.1002/celc.201901586.
[48] W. Liu, M. Ulaganathan, I. Abdelwahab, X. Luo, Z. Chen, S.J. Rong Tan, X. Wang, Y. Liu, D. Geng, Y. Bao, J. Chen, K.P. Loh, Two-dimensional polymer synthesized via solid-state polymerization for high-performance supercapacitors, ACS Nano 12 (2018) 852–860, https://doi.org/10.1021/acsnano.7b08354.
[49] Y. Kou, Y. Xu, Z. Guo, D. Jiang, Supercapacitive energy storage and electric power supply using an aza-fused π-conjugated microporous framework, Angew. Chem. Int. Ed. 123 (2011) 8912–8916, https://doi.org/10.1002/anie.201103493.
[50] H. Zhao, Y. Wang, R. Liu, W. Cheng, Y. Wu, H. Cao, F. Liang, Preparation and electrochemical properties of porous organic polymer with high ionic diffusion coefficient as cathode material for lithium-ion batteries, J. Power Sources 626 (2025) 235733, https://doi.org/10.1016/j.jpowsour.2024.235733.
[51] S.B. Xia, Y.Q. Cai, L.F. Yao, J.Y. Shi, F.X. Cheng, J.J. Liu, Z.J. He, J.C. Zheng, Nitrogen-rich two-dimensional p-conjugated porous covalent quinazoline polymer for lithium storage, Energy Storage Mater. 50 (2022) 225–233, https://doi.org/10.1016/j.ensm.2022.05.021.
[52] Q. Chen, R. Suizu, Y. Shuku, H. Omachi, M.M. Matsushita, S. Fukuura, T. Yumura, S. Bandow, K. Awaga, Unveiling π–π interactions in triptycene-phenazine/SWCNT redox chemistry using ESR spectroscopy, J. Mater. Chem. A 12 (2024) 24096–24102, https://doi.org/10.1039/D4TA04176C.
[53] Z. Liu, Z. Wang, Y. Shi, Y.M. Shen, W. Wang, Z. Chen, J. Xu, J. Cao, A high-capacity hexaazatrinaphthylene anode for aqueous organic hybrid flow batteries, J. Mater. Chem. A 9 (2021) 27028–27033, https://doi.org/10.1039/D1TA06138K.
[54] J.L. Segura, R. Juárez, M. Ramos, C. Seoane, Hexaazatriphenylene (HAT) derivatives: From synthesis to molecular design, self-organization and device applications, Chem. Soc. Rev. 44 (2015) 6850–6885, https://doi.org/10.1039/C5CS00181A.
[55] Z. Sun, H. Yao, J. Liu, Z. Lin, M. Shu, H. Liu, S. Zhu, S. Guan, Stable Hexaazatrinaphthalene-based planar polymer cathode material for organic Lithium-ion batteries, ACS Appl. Mater. Interfaces 15 (2023) 42603–42610, https://doi.org/10.1021/acsami.3c08481.
[56] Y. Wang, P. Poldorn, Y. Wongnongwa, S. Jungsuttiwong, C. Chen, L. Yu, Z. Wang, L. Shi, Y. Zhao, S. Yuan, Cobalt(II)-Hexaazatriphenylene Hexacarbonitrile coordination compounds based cathode materials with high capacity and long cycle stability, Adv. Funct. Mater. 32 (2022) 2111043, https://doi.org/10.1002/adfm.202111043.
[57] M.G. Mohamed, B. Halder, P.N. Singh, A.A.K. Mohammed, P. Elumalai, S.W. Kuo, Molecular engineering and synergistic redox-active hexaazatrinaphthalene and pyrene-based conjugated microporous polymers for superior faradaic supercapacitor energy storage, Chem. Eng. J. 520 (2025) 165892, https://doi.org/10.1016/j.cej.2025.165892.
[58] P. Xu, S. Ouyang, Q. Bai, Q. Ma, Y. Zhu, A hexaazatriphenylene-based porous organic polymer for high performance supercapacitor, J. Polym. Sci. 62 (2024) 1647–1653, https://doi.org/10.1002/pol.20230256.
[59] Q. Huang, J. Chen, X. Shao, L. Zhang, Y. Dong, W. Li, C. Zhang, Y. Ma, New electropolymerized triphenylamine polymer films and excellent multifunctional electrochromic energy storage system materials with real-time monitoring of energy storage status, Chem. Eng. J. 461 (2023) 141974, https://doi.org/10.1016/j.cej.2023.141974.
[60] R.R. Divya, S. Panday, M.E. Ali, S. Ali, R.K. Kalla, R. Pandey, Jangir, An electron rich triazine-based covalent organic framework as an aqueous electrolyte symmetric supercapacitor, Chem. Commun. 61 (2025) 7831–7834, https://doi.org/10.1039/D5CC01105A.
[61] M.M. Samy, M.G. Mohamed, S.U. Sharma, S.V. Chaganti, T.H. Mansoure, J.T. Lee, T. Chen, S.W. Kuo, Constructing conjugated microporous polymers containing triphenylamine moieties for high-performance capacitive energy storage, Polymer 264 (2023) 125541, https://doi.org/10.1016/j.polymer.2022.125541.
[62] H.C. Yang, Y.Y. Chen, S.Y. Suen, R.H. Lee, Triazine-based covalent organic framework/carbon nanotube fiber nanocomposites for high-performance supercapacitor electrodes, Polymer 273 (2023) 125853, https://doi.org/10.1016/j.polymer.2023.125853.
[63] B. Liu, L. Zhao, Y. Liu, H. Chen, H. Li, M. Yang, J. Qiu, Triazine-containing covalent organic polymer-derived grid-like Multilocular spheres for aqueous supercapacitors, Adv. Mater. 37 (2025) 2419124, https://doi.org/10.1002/adma.202419124.
[64] L. Xu, L. Zhenhu, Z. Yulin, G. Hanlin, Z. Meiying, L. Haoxiang, L. Yuping, L. Shuangyi, Stable hexaazatrinaphthylene-based covalent organic framework as high-capacity electrodes for aqueous hybrid supercapacitors, Energy Mater. 5 (2025) 500036, https://doi.org/10.20517/energymater.2024.127.

[65] J. Wang, C.S. Chen, Y. Zhang, Hexaazatrinaphthylene-based porous organic polymers as organic cathode materials for Lithium-ion batteries, ACS Sustain. Chem. Eng. 6 (2018) 1772–1779, https://doi.org/10.1021/acssuschemeng.7b03165.
[66] L. Li, F. Lu, R. Xue, B. Ma, Q. Li, N. Wu, H. Liu, W. Yao, H. Guo, W. Yang, Ultrastable triazine-based covalent organic framework with an interlayer hydrogen bonding for supercapacitor applications, ACS Appl. Mater. Interfaces 11 (2019) 26355–26363, https://doi.org/10.1021/acsami.9b06867.
[67] M. Mahato, S. Nam, R. Tabassian, S. Oh, V.H. Nguyen, I.K. Oh, Electronically conjugated multifunctional covalent triazine framework for unprecedented CO_2 selectivity and high-power flexible supercapacitor, Adv. Funct. Mater. 32 (2021) 2107442, https://doi.org/10.1002/adfm.202107442.
[68] Y. Zhang, B. Zhang, L. Chen, T. Wang, M. Di, F. Jiang, X. Xu, S. Qiao, Rational design of covalent triazine frameworks based on pore size and heteroatomic toward high performance supercapacitors, J. Colloid Interface Sci. 606 (2022) 1534–1542, https://doi.org/10.1016/j.jcis.2021.08.087.
[69] J. Huang, S. Hu, X. Yuan, Z. Xiang, M. Huang, K. Wan, J. Piao, Z. Fu, Z. Liang, Radical stabilization of a tripyridinium–triazine molecule enables reversible storage of multiple electrons, Angew. Chem. Int. Ed. 60 (2021) 20921–20925, https://doi.org/10.1002/anie.202107216.